PHYSICAL REVIEW A **108**, 023106 (2023)

Signatures of the phase structure in multiphoton ionization of aligned N_2 molecules

Zhenning Guo,[1] Peipei Ge,[1,*] Yankun Dou,[1] Mingming Liu,[1] Xiaoxiao Long,[1] Jiguo Wang,[1]
Qihuang Gong,[1,2,3] and Yunquan Liu[1,2,3,†]
[1] *State Key Laboratory for Mesoscopic Physics and Frontiers Science Center for Nano-optoelectronics,*
School of Physics, Peking University, Beijing 100871, China
[2] *Collaborative Innovation Center of Quantum Matter, Beijing 100871, China*
[3] *Collaborative Innovation Center of Extreme Optics, Shanxi University, Taiyuan, Shanxi 030006, China*

(Received 11 April 2023; revised 20 July 2023; accepted 21 July 2023; published 4 August 2023)

We experimentally measure the photoelectron momentum distributions of multiphoton ionization of aligned N_2 molecules at 400 nm. The phase structure of the ionized electron wave packet is probed with a weak parallelly polarized field at 800 nm. By inspecting the two-color phase-resolved photoelectron interference fringes, we observe a relative phase shift between the yields of above-threshold ionization and sideband peaks that depends on the molecular alignment angle. With the support of molecular strong-field approximation, we show the measured alignment-dependent relative phase shift is associated with the initial phase of electron wave packet dictated by the molecular orbital at the ionization exit, which is mapped into the intracycle interference. We find that the initial phase which depends on the molecular alignment can be modulated by the two-color synthesized fields and decreases with increasing photoelectron energy. Finally, we demonstrate the alignment-dependent phase shift in momentum space allows the retrieval of the relative spatial displacement for electrons at the ionization exit in position space between different alignments.

DOI: 10.1103/PhysRevA.108.023106

I. INTTRODUCTION

Laser-induced photoionization of atoms and molecules, as the fundamental process of light-matter interaction, has triggered a broad range of strong-field phenomena, such as high harmonic generation [1–4], above-threshold ionization (ATI) [5,6], and photoelectron holography [7–9], etc. Among these phenomena, photoelectron holography serves as a well-established technique in revealing the details of strong-field ionization [10–17], especially in uncovering the structural information of atoms and molecules [8,9,16,17], as it is associated with the recollision process. Recently, using photoelectron holography, a nontrivial phase structure of the tunneling electron wave packet in strong-field ionization of molecules has been revealed [10,11]. This phase structure is found to tightly depend on the molecular alignment and can be accounted for by the transverse spatial displacement of electrons at the ionization exit. Hence, it has important implications for imaging the molecular orbital [16–18] and probing the ionization geometry in molecules [19,20].

However, when the ionization transits to multiphoton regime, the electron rescattering would be largely suppressed. As a result, photoelectron holography disappears. Only the intercycle and intracycle interference structures of direct electron wave packets survive on photoelectron momentum distributions. Disentangling these two kinds of interference structures in the strong-field multiphoton regime has been reported in atoms, in order to time the release of electrons [21–23], monitor the temporary retrapping of photoelectrons by the atomic potential [24], and completely characterize the electron wave function [25,26]. Transferring this analysis of photoelectron interference from atoms to molecules considerably increases experimental and theoretical complexity because of the spatial distribution of electron density, i.e., the molecular orbital, which would leave a subtle fingerprint on the photoelectron interference pattern [27]. In this case, how to unravel the effect of molecular orbital from the electron interference pattern and resolve the phase structure of the electron wave packet in multiphoton ionization of molecules is essential for comprehensively understanding the laser-molecule interaction.

In this paper, we investigate the photoelectron interference fringes in multiphoton ionization of prealigned N_2 molecules and retrieve the phase structure, which encodes the spatial displacement of the emitted electron wave packet at ionization exit. Experimentally, we measure the photoelectron momentum distributions (PMDs) of parallel- and perpendicular-aligned N_2 molecules in a strong 400-nm ionizing field combined with a weak 800-nm probing field of parallel polarization. By monitoring the two-color phase-dependent photoelectron signals, we observe a relative phase shift between the yields of the ATI peak and the sideband (SB) peak that presents a considerable dependence on the molecular alignment angle. Using the molecular strong-field approximation (MOSFA) within the saddle-point approach, we attribute the alignment-dependent relative phase shift between ATI and SB peaks to the alignment-dependent initial phase carried by the electron wave packets at the ionization exit, which is also dependent on the photoelectron energy. This molecular-orbital-dictated initial phase allows the

---

*gepeipei@pku.edu.cn
†yunquan.liu@pku.edu.cn

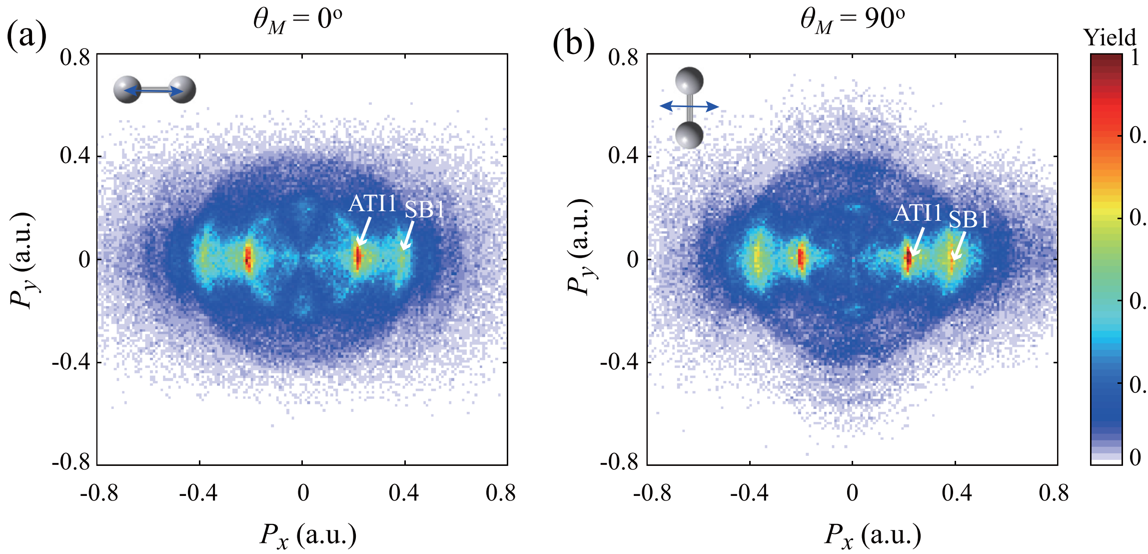

FIG. 1. (a),(b) Measured two-dimensional photoelectron momentum distributions integrated over the relative phase ϕ of the two-color fields at the 0° and 90° alignment angles.

retrieval of the relative spatial displacement of the emitted electron wave packet at the ionization exit between the parallel and perpendicular alignments.

II. EXPERIMENTAL SETUP AND RESUTLS

Experimentally, the linearly polarized femtosecond laser pulse at 800 nm is generated from a Ti:sapphire laser system (35 fs, 3 kHz). The pulse is first split into an alignment pulse ($\sim$130 fs) and an ionizing pulse ($\sim$35 fs) with variable relative delay. The alignment pulses have been stretched to $\sim$130 fs and its intensity is carefully controlled so that no apparent ionizing signal can be generated solely by the alignment pulses. The alignment angle is monitored by rotating the polarization of alignment pulses with a half-wave plate. The degree of alignment is estimated to be $\langle\cos^2\theta_M\rangle \sim 0.61$ by inspecting the Coulomb explosion events. The delayed ionizing pulse is then input into a Mach-Zehnder interferometer scheme to generate the parallelly polarized two-color (PTC) field. Here, one arm is frequency doubled to generate the second harmonic (400 nm) using a 250-μm-thick β-barium borate (β-BBO) crystal, which is used to trigger multiphoton ionization of aligned molecules. The weak fundamental pulse serves as the probing field. The relative phase ϕ between the two-color components is controlled by using a pair of fused silica wedges with the time accuracy $\sim$5 as. Both aligning pulses and ionizing two-color pulses are focused onto a cold supersonic gas beam of N_2 by a silver concave mirror ($f = 75$ mm). The three-dimensional momentum distributions of the fragment ions and the electrons are detected using a cold target recoil ion momentum spectroscopy (COLTRIMS) [28]. The intensity of the 400-nm field is calibrated to be $\sim 1.1 \times 10^{14}$ W/cm^2 ($E_{400} \sim 0.04$ a.u.) according to the locations of ATI peaks. The intensity of 800-nm field is calibrated to be $\sim 1.1 \times 10^{12}$ W/cm^2 ($E_{800} \sim 0.004$ a.u.) by the solution of two-dimensional time-dependent Schrödinger equation (TDSE) [29].

In Figs. 1(a) and 1(b), we show the measured PMDs of aligned N_2 molecules at 0° and 90° in the PTC field. Here the PMDs are integrated with the relative phase of the PTC fields, and the electrons are limited within a momentum slice $|p_z| < 0.1$ a.u. (p_z is the electron momentum along the laser propagation direction). As can be seen, the PMDs at the two alignment angles are dominated by a series of ring structures, which correspond to the alternating ATI and sideband peaks. Two prominent rings in the PMDs are assigned to the first-order ATI (ATI1) peak at $p_x \sim \pm 0.21$ a.u. and the first-order SB (SB1) peaks at $p_x \sim \pm 0.39$ a.u. Owing to the imperfect alignment in the experiments, the phase-integrated PMDs of the parallel and perpendicular alignments are almost indistinguishable except for the slight difference on the fine node structures of the ATI1 rings.

In order to reveal the phase structure imprinted in the interference pattern, we transform the momentum distributions into the energy spectra and inspect the measured photoelectron energy spectra as a function of the relative phase of two-color fields, as shown in Fig. 2. Here, the synthesized two-color field can be expressed as $\mathbf{E}(t) = [E_{400}\cos(2\omega t) + E_{800}\cos(\omega t + \phi)]\mathbf{x}$. One can observe that the yields of both ATI1 and SB1 peaks experience periodic oscillations with respect to the relative phase ϕ of the two-color field. For clear visualization, we extract the photoelectron yield oscillations of ATI1 and SB1 peaks (the integration width is about 0.8 eV which corresponds to the width of the energy peaks). The results are shown in Figs. 2(c) and 2(d) for $\theta_M = 0^\circ$ and $\theta_M = 90^\circ$ cases, respectively. Each yield oscillation of ATI1 and SB1 peaks has been fitted by $Y = A + B\cos(\phi - \alpha)$. Here α is the phase offset of oscillating modulations. To identify the effect of molecular alignment on the two-color phase-dependent photoelectron signals, we focus on the relative phase shift between the ATI1 and SB1. For the $\theta_M = 0^\circ$ case, the relative phase shift of ATI1 and SB1 is $\Delta\alpha_0 = \alpha_0^{\mathrm{SB1}} - \alpha_0^{\mathrm{ATI1}} = 1.30$ rad. For the $\theta_M = 90^\circ$ case, $\Delta\alpha_{90} = \alpha_{90}^{\mathrm{SB1}} - \alpha_{90}^{\mathrm{ATI1}} =$

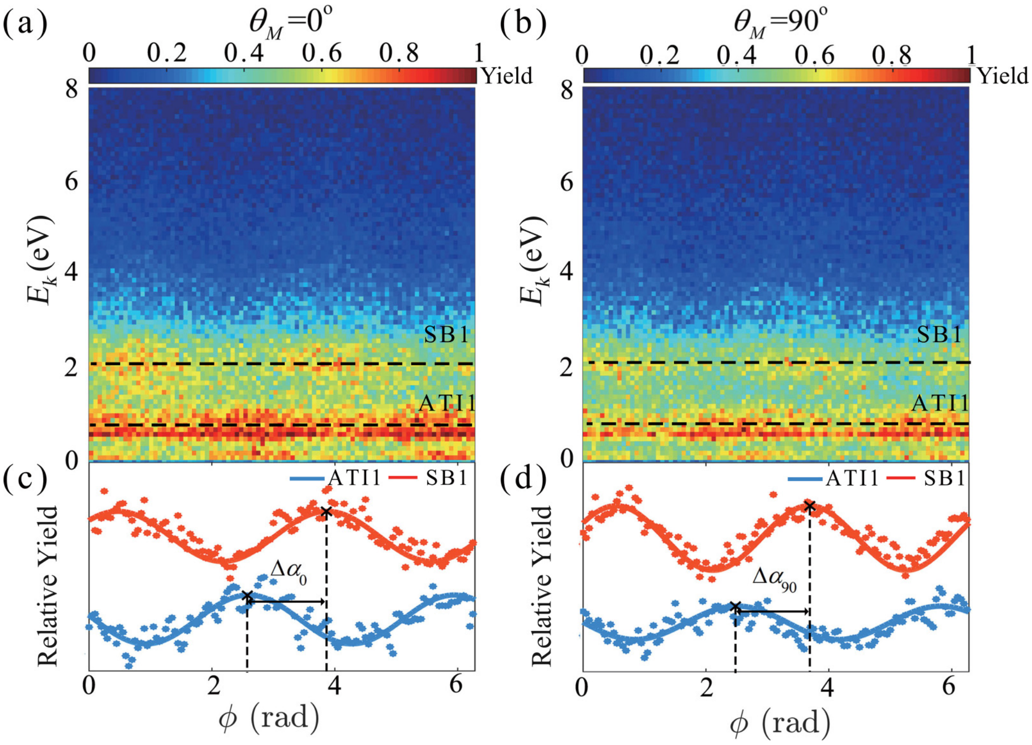

FIG. 2. (a),(b) Measured photoelectron energy distributions with respect to the relative phase ϕ of the two-color fields at 0° and 90° alignment angles. (c),(d) Yield oscillations of ATI1 and SB1 peaks as a function of relative phase ϕ at 0° and 90° alignment angles.

1.18 rad. The difference between the parallel and perpendicular geometries is $\delta\alpha_{0/90} = \Delta\alpha_0 - \Delta\alpha_{90} = 0.12$ rad. This suggests the molecular-alignment-dependent two-color modulated photoelectron interference, which might encode the phase structure in multiphoton ionization of N_2. Resolving this phase would help us to better understand the influence of the molecular orbital on strong-field ionization of molecules.

III. THEORETICAL ANALYSIS

To model the experiment, we first numerically solve the two-dimensional TDSE for N_2 in the PTC fields (see Appendix A for a detailed description) [29,30]. In the simulation, we use a perfect alignment. The calculated two-color phase-dependent energy spectra for parallel and perpendicular alignments are shown in Figs. 3(a) and 3(b), respectively. From these results, we extract the relative phase shifts between ATI1 and SB1 for $\theta_M = 0°$ and 90°, which are $\Delta\alpha_0 = \alpha_0^{\mathrm{SB1}} - \alpha_0^{\mathrm{ATI1}} = 1.35$ rad and $\Delta\alpha_{90} = \alpha_{90}^{\mathrm{SB1}} - \alpha_{90}^{\mathrm{ATI1}} = 1.21$ rad. The difference between the parallel and perpendicular geometries is $\delta\alpha_{0/90} = \Delta\alpha_0 - \Delta\alpha_{90} = 0.14$ rad. The solution of TDSE agrees well with the experimental measurement, validating the experimental observation of the alignment-dependent relative phase shift between the photoelectron interference fringes.

To figure out the origin of alignment-dependent relative phase shift, we turn to molecular strong-field approximation (MOSFA) [31–34]. Within the saddle-point approach, the transition amplitude $M(\mathbf{p}, \theta_M)$ of electrons with the final momentum $\mathbf{p}$ from the molecular ground state $\Psi_{N_2}(\mathbf{r})$ to the final Volkov state can be expressed as the coherent superposition of quantum orbits $M_j(\mathbf{p}, \theta_M)$,

$$M(\mathbf{p},\theta_M) = \sum_j M_j(\mathbf{p},\theta_M) = \sum_j D_s^{(j)}(\mathbf{p},\theta_M)e^{iS(\mathbf{p},t_s^{(j)})}. \quad (1)$$

Here, $t_s^{(j)}$ is the saddle point which satisfies the saddle-point equation $[\mathbf{p}+\mathbf{A}(t_s^{(j)})]^2/2 + I_p = 0$. It represents the ionization instant of the quantum orbit. The pre-exponential term that encodes the molecular orbital structure reads

$$D_s^{(j)}(\mathbf{p},\theta_M) = \langle \mathbf{p}+\mathbf{A}(t_s^{(j)}) | \mathbf{r}\cdot\mathbf{E}(t_s^{(j)}) | \Psi_{N_2}(\mathbf{r})\rangle. \quad (2)$$

Here, $\mathbf{A}(t)$ is the vector potential of the laser field. θ_M is the molecular alignment angle, and I_p is the ionization potential. $S(\mathbf{p}, t_s^{(j)}) = \int_{t_s^{(j)}}^{\infty} d\tau\{[\mathbf{p}+\mathbf{A}(\tau)]^2/2 + I_p\}$ is the complex phase of quantum orbit. According to the transition amplitude in Eq. (1), the total phase structure $\beta_{\theta_M}^{(j)} = \arg[M_j(\mathbf{p},\theta_M)]$ of the emitted electron wave packet is composed of two terms,

$$\beta_{\theta_M}^{(j)} = \arg\left[D_s^{(j)}(\mathbf{p},\theta_M)\right] + \mathrm{Re}\left[S(\mathbf{p},t_s^{(j)})\right] = \varepsilon_{\theta_M}^{(j)} + s^{(j)}. \quad (3)$$

Here, $\varepsilon_{\theta_M}^{(j)} = \arg[D_s^{(j)}(\mathbf{p},\theta_M)]$ corresponds to the initial phase of electron at the ionization exit and tightly depends on the molecular alignment angle θ_M [12,35]. $s^{(j)} = \mathrm{Re}[S(\mathbf{p}, t_s^{(j)})]$ is the field-induced phase that is independent of θ_M [36,37]. More details of the MOSFA model can be found in Appendix B.

In Figs. 4(a) and 4(b), we show the calculated photoelectron energy spectra as a function of the relative phase ϕ for $\theta_M = 0°$ and $\theta_M = 90°$ using the MOSFA model, respectively. Likewise, we also extract the yield oscillations of ATI1 and SB1 peaks from the calculated photoelectron energy

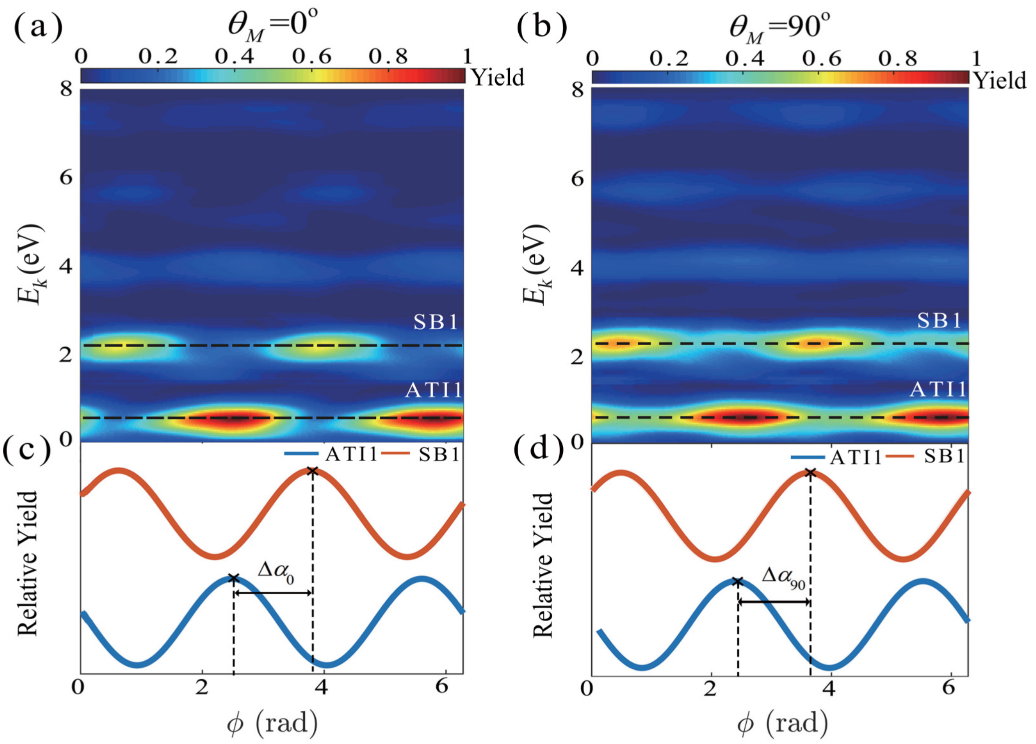

FIG. 3. (a),(b) Simulated photoelectron energy distributions with respect to the relative phase ϕ using TDSE at 0° and 90° alignment angle. (c),(d) Photoelectron yield oscillation of ATI1 and SB1 peaks as a function of relative phase ϕ at 0° and 90° alignment angles, respectively.

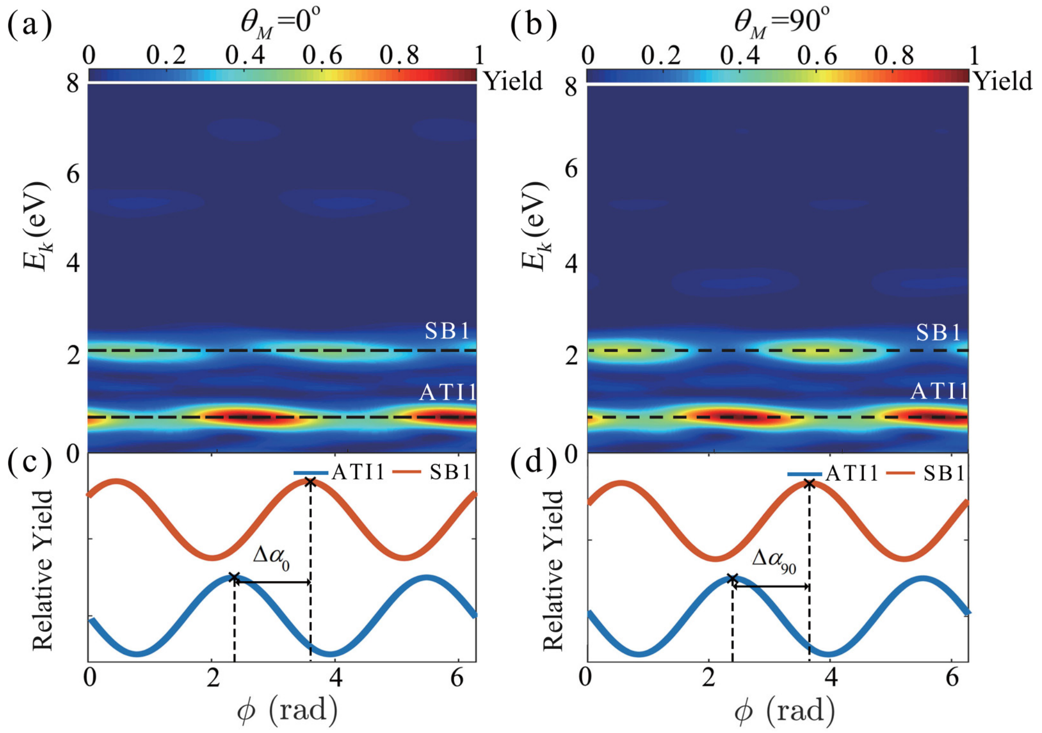

FIG. 4. (a),(b) Simulated photoelectron energy distributions with respect to the relative phase ϕ using MOSFA at 0° and 90° alignment angles. (c),(d) photoelectron yield oscillation of ATI1 and SB1 peaks as a function of relative phase ϕ at 0° and 90° alignment angles, respectively.

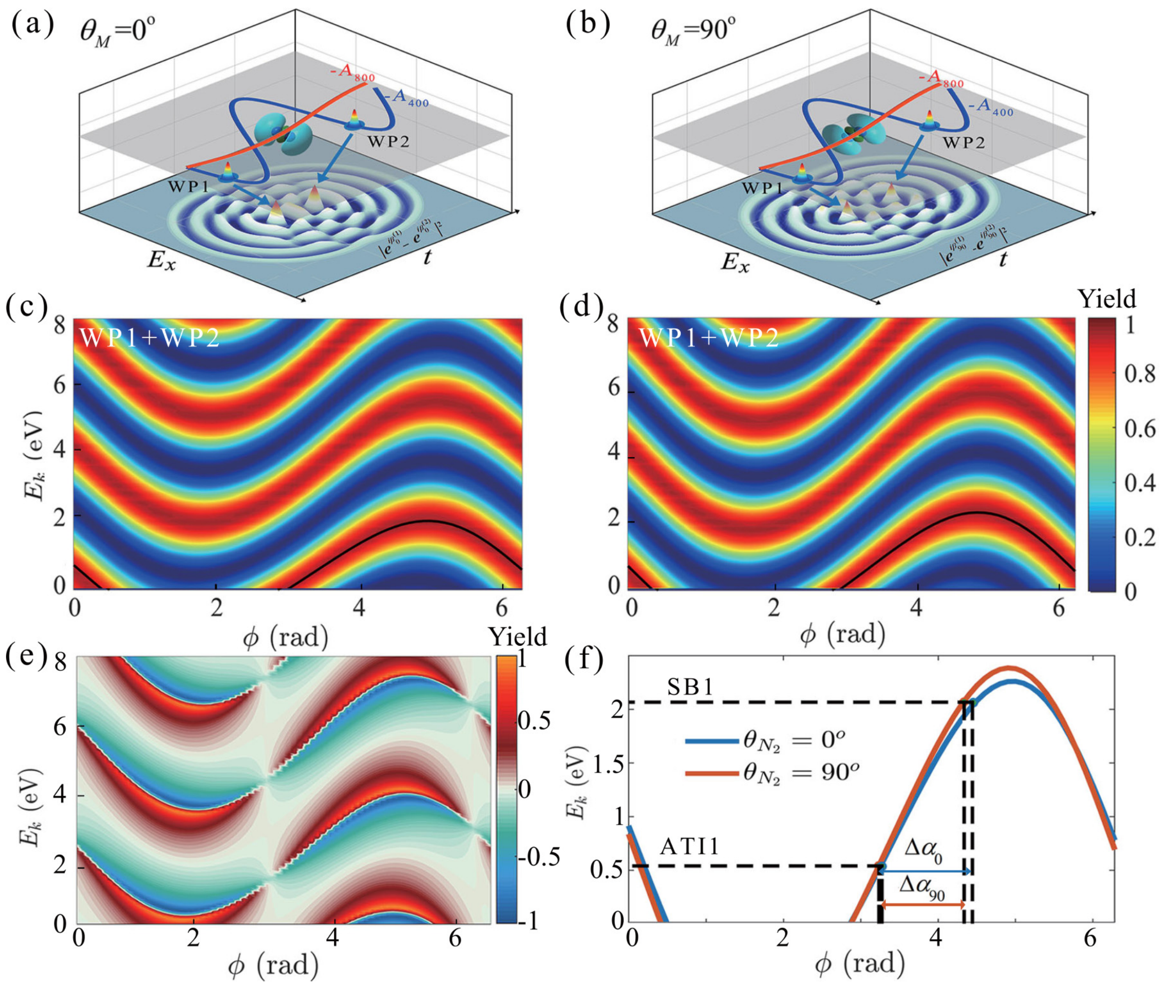

FIG. 5. (a),(b) Graphical representation of the intracycle interference between electron wave packet 1 (WP1) and wave packet 2 (WP2) for $\theta_M = 0^\circ$ and $\theta_M = 90^\circ$ cases. (c),(d) Intracycle interference of WP1 and WP2 as a function of the relative phase ϕ and electron energy for $\theta_M = 0^\circ$ and $\theta_M = 90^\circ$ cases. (e) Normalized differential intracycle interference between $\theta_M = 0^\circ$ and $\theta_M = 90^\circ$ cases. (f) Extracted most probable energy curves of the first-order intracycle interference fringes, which are indicated by the black lines in panels (c) and (d). The electron energies of ATI1 and SB1 peaks are indicated by the black dashed lines.

spectra, as shown in Figs. 4(c) and 4(d). For the $\theta_M = 0^\circ$ case [Fig. 4(c)], the extracted relative phase shift $\Delta\alpha_0 = 1.40$ rad. For the $\theta_M = 90^\circ$ case [Fig. 4(d)], $\Delta\alpha_{90} = 1.29$ rad. The difference between the parallel and perpendicular geometries $\delta\alpha_{0/90} = 0.11$ rad. It is evident that the MOSFA calculations basically reproduce the alignment-dependent phase shift of experiment and TDSE simulation. As for the larger relative phase shifts $\Delta\alpha_0$ and $\Delta\alpha_{90}$, it might result from the neglect of the long-range tail of the molecular Coulomb potential in the MOSFA.

Within the MOSFA, the electron interference pattern can be decomposed as the supposition of two types of electron interference, i.e., intercycle and intracycle interferences [38]. Considering the periodicity of the two-color synthesized field, the electron wave packets that are emitted at the ionization instants separated by 800-nm cycles give rise to the intercycle interference, which manifests as the 800-nm ATI peaks and accounts for the emergence of the SB peaks in two-color fields. For this interference, the electron wave packets are released in the same electric field [e.g., $\mathbf{E}(t_s^{(j)}) = \mathbf{E}(t_s^{(j)} + T_{800})$ and $\mathbf{A}(t_s^{(j)}) = \mathbf{A}(t_s^{(j)} + T_{800})$] and thus they have the same initial phase ε_{θ_M} [see Eq. (2)]. When these electron wave packets interfere, the effect of the alignment-dependent initial phase would be eliminated. Consequently, the intercycle interference is independent of the molecular alignment angle θ_M and the relative phase ϕ.

For the intracycle interference, it corresponds to the interference between the two electron wave packets emitted from adjacent 400-nm cycles [abbreviated as wave packet 1 (WP1) and wave packet 2 (WP2) in Figs. 5(a) and 5(b)] with their ionization instants labeled as $t_s^{(\mathrm{WP1})}$ and $t_s^{(\mathrm{WP2})}$. In single 400-nm fields, $t_s^{(\mathrm{WP2})} = t_s^{(\mathrm{WP1})} + T_{400}$, while in two-color fields, at these two instants, the 800-nm electric field points to the opposite direction. As a result, the emitted two electron wave packets would experience opposite modulations induced by the weak 800-nm laser field. In this case $\mathbf{E}(t_s^{(\mathrm{WP1})}) \neq \mathbf{E}(t_s^{(\mathrm{WP2})})$ and $\mathbf{A}(t_s^{(\mathrm{WP1})}) \neq \mathbf{A}(t_s^{(\mathrm{WP2})})$. WP1 and WP2 would carry different initial phases ($\varepsilon_{\theta_M}^{(\mathrm{WP1})} \neq \varepsilon_{\theta_M}^{(\mathrm{WP2})}$) at the ionization exit. This leads to the molecular-alignment-dependent intracycle interference. For simplification, we normalize the amplitude of electron wave packet (e.g., $|M_j(\mathbf{p}, \theta_M)| = 1$), then the intracycle interference of WP1 and WP2 can be

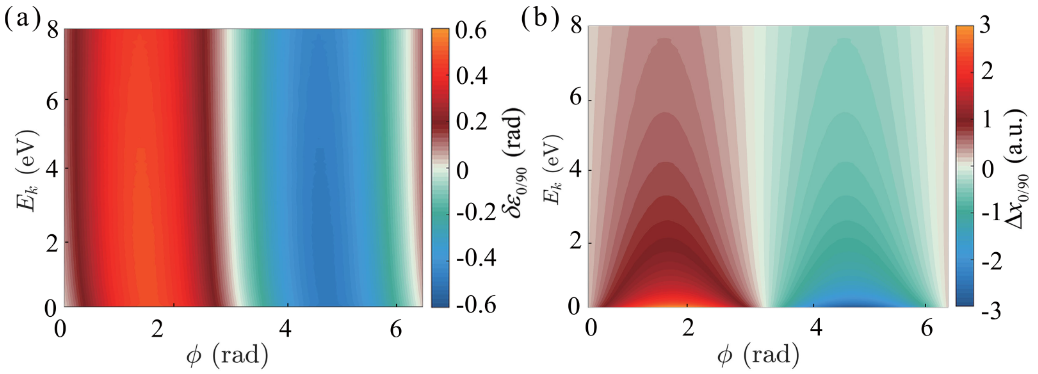

FIG. 6. (a) Relative phase shift $\delta\varepsilon_{0/90}$ as a function of electron energy E_k and the relative phase ϕ. Here $\delta\varepsilon_{0/90} = \Delta\varepsilon_0 - \Delta\varepsilon_{90}$, with $\Delta\varepsilon_0$ and $\Delta\varepsilon_{90}$ the initial phase difference between WP1 and WP2 for $\theta_M = 0^\circ$ ($\theta_M = 90^\circ$) case. (b) Relative spatial displacement $\Delta x_{0/90}$ of electrons in position space as a function of the relative phase ϕ and electron energy E_k.

written as

$$\left| e^{i\beta_{\theta_M}^{(\mathrm{WP1})}} + e^{i\beta_{\theta_M}^{(\mathrm{WP2})}} \right| \sim \cos\left(\beta_{\theta_M}^{(\mathrm{WP1})} - \beta_{\theta_M}^{(\mathrm{WP2})}\right) \sim \cos\left(\Delta\beta_{\theta_M}\right). \tag{4}$$

Here, $\Delta\beta_{\theta_M} = (\varepsilon_{\theta_M}^{(\mathrm{WP1})} - \varepsilon_{\theta_M}^{(\mathrm{WP2})}) + (s^{(\mathrm{WP1})} - s^{(\mathrm{WP2})})$ represents the phase difference of intracycle interference. Based on Eq. (4), we calculate the intracycle interference patterns for the alignment angles $\theta_M = 0^\circ$ and $\theta_M = 90^\circ$. The corresponding results are shown in Figs. 5(c) and 5(d), respectively. Discrete interference fringes that are separated by one 400-nm photon energy can be clearly observed. And these fringes are oscillating as a function of the relative phase ϕ. To resolve the alignment dependence of the phase-dependent intracycle interference, we present the normalized differential interference spectrum with $[M(E_k, \theta_M = 90^\circ) - M(E_k, \theta_M = 0^\circ)]/[M(E_k, \theta_M = 0^\circ) + M(E_k, \theta_M = 90^\circ)]$ in Fig. 5(e), where $M(E_k, \theta_M = 0^\circ)$ and $M(E_k, \theta_M = 90^\circ)$ respectively represent the interference patterns for parallel and perpendicular alignments as shown in Figs. 5(c) and 5(d). The differential spectrum directly confirms the alignment-dependent features of the intracycle interference. Besides, the normalized differential interference fringes exhibit prominent dependencies on the two-color relative phase and the photoelectron energy.

In Fig. 5(f), we extract the most probable electron energy E_k of the first-order intracycle interference fringe for parallel and perpendicular molecular alignments [indicated by the black lines in Figs. 5(c) and 5(d)]. It is evident that, besides the difference in the oscillating amplitude of the interference fringes, the peak position of the interference fringe in $\theta_M = 0^\circ$ case has a slight offset with respect to the case of $\theta_M = 90^\circ$. Then we extract the phases ϕ of the intracycle interference for the selected electron energy E_k (respectively corresponding to ATI1 and SB1 peaks) and calculate the relative phase shift for ATI1 and SB1 peaks. The extracted $\Delta\alpha_0$ and $\Delta\alpha_{90}$ are in excellent agreement with the results of MOSFA model (Fig. 4). This means that the alignment-dependent phase shift between the ATI1 and SB1 peaks is associated with the alignment-dependent intracycle interference, which can be modulated by the weak 800-nm field and depends on the photoelectron energy.

In the next step, we resolve the subtle initial phase of electrons from the molecular alignment-dependent intracycle interference. As governed by Eq. (4), the difference of the intracycle-interference phase between the parallel and perpendicular alignments can be written as

$$\begin{aligned}\delta\beta_{0/90} &= \Delta\beta_0 - \Delta\beta_{90}\\ &= \left(\varepsilon_0^{(\mathrm{WP1})} - \varepsilon_0^{(\mathrm{WP2})}\right) + (s^{(\mathrm{WP1})} - s^{(\mathrm{WP2})})]\\ &\quad - \left[\left(\varepsilon_{90}^{(\mathrm{WP1})} - \varepsilon_{90}^{(\mathrm{WP2})}\right) + (s^{(\mathrm{WP1})} - s^{(\mathrm{WP2})})\right]\\ &= \left[\varepsilon_0^{(\mathrm{WP1})} - \varepsilon_0^{(\mathrm{WP2})}\right] - \left[\varepsilon_{90}^{(\mathrm{WP1})} - \varepsilon_{90}^{(\mathrm{WP2})}\right]\\ &= \delta\varepsilon_{0/90}.\end{aligned} \tag{5}$$

Here the alignment-independent field-induced phase term $s^{(j)}$ can be erased and the difference of the initial phase between parallel and perpendicular alignments is revealed. Figure 6(a) displays the difference of the intracycle-interference phase $\delta\varepsilon_{0/90}$ as a function of the relative phase ϕ and electron energy E_k. One can see that $\delta\varepsilon_{0/90}$ vanishes at $\phi = \pi$ and $\phi = 2\pi$ because of the vanishing modulation of the 800-nm laser field, and the magnitude of $\delta\varepsilon_{0/90}$ slightly decreases with increasing electron energy E_k. As the initial phase results from the transition of bound electrons from the molecular orbital to the continuum state by absorption of photons, the phase difference $\delta\varepsilon_{0/90}$ also reflects the discrepancy in photoemission dynamics between parallel and perpendicular alignments. From the perspective of the Fourier transform, the relative phase shift of the electron wave functions between parallel and perpendicular alignments in momentum space corresponds to the relative spatial displacement in position space (the momentum space and the position space are linked by Fourier transformation; also see Refs. [39–41]). In the momentum space, the electron wave functions in parallel and perpendicular alignments satisfy $\Phi_0(p) = \Phi_{90}(p)e^{i\delta\varepsilon_{0/90}}$. According to the Fourier transformation, the electron wave functions in position space at the two alignment angles could be governed by

$$\Psi_0(x) = \Psi_{90}(x + \delta\varepsilon_{0/90}\hbar/p) = \Psi_{90}(x + \Delta x_{0/90}). \tag{6}$$

Here $\Delta x_{0/90} = \delta\varepsilon_{0/90}\hbar/p = \delta\varepsilon_{0/90}\hbar/\sqrt{2E_k}$ represents the relative spatial displacement of the electrons between parallel and perpendicular alignments at the ionization exit. Based on the result of $\delta\varepsilon_{0/90}$ as shown in Fig. 6(a), we further obtain the two-color phase- and energy-dependent $\Delta x_{0/90}$ as displayed in Fig. 6(b). Clearly, one can see that the relative spatial displacement of electrons at the ionization exit between parallel and perpendicular alignments evolves from a negative value of -3 a.u. at $\phi = 1.57$ rad to a positive value of 3 a.u. at $\phi = 4.71$ rad. And the magnitude of $\Delta x_{0/90}$ decreases with increasing electron energy E_k.

IV. CONCLUSION

In summary, we have measured the photoelectron energy spectra of multiphoton ionization of aligned N_2 molecules and resolved the signatures of the initial phase from the alignment-dependent photoelectron interference fringes using the parallel two-color fields. Building on the analytical saddle-point MOSFA model, we have demonstrated that the observed alignment-dependent relative phase shift between ATI and SB results from the intracycle interference of emitted electron wave packets, which encodes the subtle initial phase dictated by the molecular orbital during photoionization of N_2. We show that the initial phase of emitted electron wave packets can be modulated by the two-color synthesized laser fields and allows the reconstruction of the relative spatial displacement of the electrons at the ionization exit between different molecular alignments. This study provides direct insight into the effect of molecular orbital on strong-field ionization of molecules and can be used to further explore the phase structure of strong-field ionization of complex molecules.

ACKNOWLEDGMENTS

We acknowledge the support of the National Key Research and Development Program of China (Grant No. 2022YFA1604301), National Science Foundation of China (Grants No. 92050201 and No. 8200906472), and China Postdoctoral Science Foundation (Grant No. 8206300495).

APPENDIX A: TDSE CALCULATION

We numerically solve the two-dimensional TDSE with the single-active-electron approximation for the N_2 molecule, which is given by [atomic units (a.u.) are used throughout unless stated otherwise] [29]

$$i\frac{\partial}{\partial t}\Psi(\mathbf{r},t) = \left(-\frac{\nabla^2}{2} + V(\mathbf{r}) + \mathbf{r}\cdot\mathbf{E}(t)\right)\Psi(\mathbf{r},t), \tag{A1}$$

where $\Psi(\mathbf{r},\ t)$ represents the electron wave function and $\mathbf{r} = (x,\ y)$ denotes the electron position in the polarization plane. $V(\mathbf{r})$ is the effective soft-core potential with

$$V(\mathbf{r}) = -\sum_{J=1}^{2}\frac{Z_J^{\infty} + \left(Z_J^0 - Z_J^{\infty}\right)\exp(-|\mathbf{r}-\mathbf{R}_J|^2/\sigma^2)}{\sqrt{|\mathbf{r}-\mathbf{R}_J|^2 + a^2}}. \tag{A2}$$

Here $J = 1, 2$ labels the nuclei at fixed position $\mathbf{R}_J$. For N_2, the bare charge parameter $Z_J^0 = 0.5$ and the effective nuclear charge $Z_J^{\infty} = 7$, respectively. The soft-core parameter a and the effective charge shielding parameter σ are chosen to match the highest occupied molecular orbital (HOMO) of N_2. Here, we choose $a = 1.2$ and $\sigma = 0.833$.

The wave function is propagated using the splitting-operator method [42]. The initial wave function is prepared by imaginary-time propagation. For the real-time propagation of the initial wave function, we split the electron wave function $\Psi(\mathbf{r},\ t_i)$ at each time step t_i into the inner-bound part $\Psi_{\text{bound}}(\mathbf{r},\ t_i)$ and the ionizing part $\Psi_{\text{ionizing}}(\mathbf{r},\ t_i)$ by a smooth absorbing function. Then we transform the ionizing part $\Psi_{\text{ionizing}}(\mathbf{r},\ t_i)$ into momentum space $\Phi_{\text{ionizing}}(\mathbf{p},\ t_i)$ and propagate the ionizing wave packet under the Volkov Hamiltonian into the end of the laser pulse. Finally we obtain the photoelectron momentum distribution by the sum of the ionizing wave packet $|\Sigma_i\Phi_{\text{ionizing}}(\mathbf{p},\ t_{\text{end}},\ t_i)|^2$. The calculated two-color phase-resolved photoelectron energy spectra using TDSE for the parallel and perpendicular alignments are shown in Fig. 3.

APPENDIX B: MOLECULAR STRONG-FIELD APPROXIMATION MODEL

To gain further physical insight, we resort to the molecular strong-field approximation (MOSFA). The direct ionization transition amplitude of the photoelectron is given by [31]

$$M(\boldsymbol{p}) = -i\int_{t_0}^{t_f} dt\langle\boldsymbol{p}+\boldsymbol{A}(t)|\mathbf{r}\cdot\boldsymbol{E}(t)\big|\Psi_{N_2}(\mathbf{r})\big\rangle e^{iS(t)}. \tag{B1}$$

Here $\Psi_{N_2}(\mathbf{r})$ is the bound initial state of N_2 and $\mathbf{p}$ is the canonical momentum. The interaction of molecules with the laser field takes place between the times t_0 and t_f. $\mathbf{E}(t)$ and $\mathbf{A}(t)$ are the electric field and vector potential of the two-color linearly polarized laser fields, respectively. $S(t)$ is the classical action during ionization,

$$S(t) = \int_t^{t_f} d\tau\{[\mathbf{p}+\mathbf{A}(\tau)]^2/2 + I_p\}. \tag{B2}$$

Here the ionization potential of N_2 is $I_p = 15.58$ eV. If we use the bound-state wave function in the momentum space $\Phi_{N_2}(\mathbf{p})$, the matrix element in Eq. (3) can be calculated easily:

$$\langle\boldsymbol{p}+\boldsymbol{A}(t)|\boldsymbol{r}\cdot\boldsymbol{E}(t)\big|\Psi_{N_2}\big\rangle = i\boldsymbol{E}(t)\cdot\nabla_{\boldsymbol{k}}\Phi_{N_2}(\boldsymbol{k})|_{\boldsymbol{k}=\boldsymbol{p}+\boldsymbol{A}(t)}. \tag{B3}$$

Introducing Eq. (B3) into (B1), the transition amplitude becomes

$$M(\mathbf{p}) = \int_0^{T_p} dt\big[\mathbf{E}(t)\cdot\nabla_{\mathbf{k}}\Phi_{N_2}(\mathbf{k})e^{iS(t)}\big]|_{\mathbf{k}=\mathbf{p}+\mathbf{A}(t)}. \tag{B4}$$

For N_2 molecules, the two-centered one-electron HOMO can be derived from symmetric superposition of one-electron hydrogenlike s orbitals [11]:

$$\Phi_{N_2}(\mathbf{k}) = \frac{4\gamma^{5/2}}{\pi(k^2+\gamma^2)^2} = \frac{\cos(\mathbf{k}\cdot\mathbf{R}_0/2)}{\sqrt{1+S(R_0)}}. \tag{B5}$$

Here the equilibrium internuclear distance of N_2 is $R_0 = 2.068$ a.u. $\gamma = \sqrt{2I_p}$. $S(R_0)$ is the atomic orbital overlap integral.

Using the saddle-point approximation, the time integral in Eq. (B4) can be approximately calculated by [43]

$$\begin{aligned} M(\mathbf{p}) = -i^{q+1}\sum_j\sqrt{\frac{2\pi}{-i\ddot{S}\big(t_s^{(j)}\big)}}\frac{\Gamma(q/2)}{2\Gamma(q)}D\big(\mathbf{k},t_s^{(j)}\big) \\ \times\big[-2i\ddot{S}\big(t_s^{(j)}\big)\big]^{q/2}e^{iS(t_s^{(j)})}, \end{aligned} \tag{B6}$$

where q is the order of the pole and $D(\mathbf{k}, t_s^{(j)}) = \lim_{t\to t_s^{(j)}} i(t-t_s^{(j)})^q \mathbf{E}(t)\cdot\nabla_{\mathbf{k}}\Phi_{N_2}(\mathbf{k})$. The saddle point $t_s^{(j)}$ is obtained by solving the saddle-point equation,

$$\dot{S}\big(t_s^{(j)}\big) = \big[\mathbf{p} + \mathbf{A}\big(t_s^{(j)}\big)\big]^2/2 + I_p = 0. \tag{B7}$$

The pole originates from the fact that the momentum-space wave function of N_2 in Eq. (B5) has a pole at the saddle point $t_s^{(j)}$. In our simulation, the electric field and vector potential of the synthesized two-color linearly polarized laser fields are given by

$$\mathbf{A}(t) = A_x(t)\mathbf{e}_x = -\left(\frac{E_{800}}{\omega}\sin(\omega t) + \frac{E_{400}}{2\omega}\sin(2\omega t+\phi)\right)\mathbf{e}_x, \tag{B8}$$

$$\mathbf{E}(t) = E_x(t)\mathbf{e}_x = [E_{800}\sin(\omega t) + E_{400}\sin(2\omega t+\phi)]\mathbf{e}_x. \tag{B9}$$

Here ω is the angular frequency of light at 800 nm, and ϕ is the relative phase between the two-color components. We define the angle with respect to the x axis as the molecular orientation θ_M. Then $D(\mathbf{k}, t_s^{(j)})$ can be expressed as

$$D\big(\mathbf{k}, t_s^{(j)}\big) = \lim_{t\to t_s^{(j)}} \big(t - t_s^{(j)}\big)^q E_x(t) \times \left(\frac{\partial\Phi_{N_2}(\mathbf{k})}{\partial k_x}\cos\theta_M - \frac{\partial\Phi_{N_2}(\mathbf{k})}{\partial k_y}\sin\theta_M\right). \tag{B10}$$

Inserting the molecular wave function of Eq. (B5) into Eq. (B10), we can obtain

$$D\big(\boldsymbol{k}, t_s^{(j)}\big) = \frac{16}{\pi\ddot{S}(t_s)\sqrt{[1+S(R_0)]}} \times \cos(\mathbf{k}\cdot\mathbf{R}/2)$$
$$[6pt] \times [E_x(t_s)k_x\cos\theta_M - E_x(t_s)k_y\sin\theta_M]. \tag{B11}$$

Combing Eq. (B11) with Eq. (B6), the transition amplitude is rewritten as

$$\begin{aligned} M(\mathbf{p}) &= \sum_j M\big(t_s^{(j)}, \theta_M\big) \\ &= \sum_j M_{\text{field}}\big(t_s^{(j)}, \theta_M\big) \times M_{mo}\big(t_s^{(j)}, \theta_M\big), \end{aligned} \tag{B12}$$

with

$$M_{\text{field}}\big(t_s^{(j)}, \theta_M\big) = 2\sqrt{2\pi}\, i^{3/2}\ddot{S}^{1/2}e^{iS(t_s^{(j)})}, \tag{B13}$$

$$\begin{aligned} M_{mo}\big(t_s^{(j)}, \theta_M\big) = \big\{&\cos(\mathbf{k}\cdot\mathbf{R}/2)\big[E_x\big(t_s^{(j)}\big)k_x\cos\theta_M \\ &- E_x\big(t_s^{(j)}\big)k_y\sin\theta_M\big]\big\}. \end{aligned} \tag{B14}$$

Here, $M(t_s^{(j)}, \theta_M)$ is amplitude of the ionized electron wave packet emitted from the saddle point $t_s^{(j)}$. The total phase of the ionized electron wave packet can be expressed as $\beta_{\theta_M}^{(j)} = \arg[M_j(\mathbf{p}, \theta_M)]$.

---

[1] M. Ferray, A. L'Huillier, X. F. Li, L. A. Lompré, G. Mainfray, and C. Manus, J. Phys. B **21**, L31 (1988).

[2] J. L. Krause, K. J. Schafer, and K. C. Kulander, Phys. Rev. Lett. **68**, 3535 (1992).

[3] Y. Mairesse, A. de Bohan, L. J. Frasinski, H. Merdji, L. C. Dinu, P. Monchicourt, P. Breger, M. Kovačev, R. Taïeb, B. Carré, H. G. Muller, P. Agostini, and P. Salières, Science **302**, 1540 (2003).

[4] F. Krausz and M. Ivanov, Rev. Mod. Phys. **81**, 163 (2009).

[5] P. Agostini, F. Fabre, G. Mainfray, G. Petite, and N. K. Rahman, Phys. Rev. Lett. **42**, 1127 (1979).

[6] M. Li, J. W. Geng, H. Liu, Y. Deng, C. Wu, L. Y. Peng, Q. Gong, and Y. Liu, Phys. Rev. Lett. **112**, 113002 (2014).

[7] Y. Huismans, A. Rouzée, A. Gijsbertsen, J. H. Jungmann, A. S. Smolkowska, P. S. W. M. Logman, F. Lépine, C. Cauchy, S. Zamith, T. Marchenko, J. M. Bakker, G. Berden, B. Redlich, A. F. G. van der Meer, H. G. Muller, W. Vermin, K. J. Schafer, M. Spanner, M. Yu. Ivanov, O. Smirnova *et al.*, Science **331**, 61 (2011).

[8] X. B. Bian and A. D. Bandrauk, Phys. Rev. Lett. **108**, 263003 (2012).

[9] M. Haertelt, X.-B. Bian, M. Spanner, A. Staudte, and P. B. Corkum, Phys. Rev. Lett. **116**, 133001 (2016).

[10] M. Meckel, A. Staudte, S. Patchkovskii, D. M. Villeneuve, P. B. Corkum, R. Dörner, and M. Spanner, Nat. Phys. **10**, 594 (2014).

[11] M. M. Liu, M. Li, C. Wu, Q. Gong, A. Staudte, and Y. Liu, Phys. Rev. Lett. **116**, 163004 (2016).

[12] M. He, Y. Li, Y. Zhou, M. Li, W. Cao, and P. Lu, Phys. Rev. Lett. **120**, 133204 (2018).

[13] J. Tan, Y. Zhou, M. He, Y. Chen, Q. Ke, J. Liang, X. Zhu, M. Li, and P. Lu, Phys. Rev. Lett. **121**, 253203 (2018).

[14] G. Porat1, G. Alon, S. Rozen, O. Pedatzur, M. Krüger, D. Azoury, A. Natan, G. Orenstein, B. D. Bruner, M. J. J. Vrakking, and N. Dudovich, Nat. Commun. **9**, 2805 (2018).

[15] M. Li, H. Xie, W. Cao, S. Luo, J. Tan, Y. Feng, B. Du, W. Zhang, Y. Li, Q. Zhang, P. Lan, Y. Zhou, and P. Lu, Phys. Rev. Lett. **122**, 183202 (2019).

[16] S. G. Walt, N. B. Ram, M. Atala, N. I. Shvetsov-Shilovski, A. von Conta, D. Baykusheva, M. Lein, and H. J. Wörner, Nat. Commun. **8**, 15651 (2017).

[17] H. P. Kang, A. S. Maxwell, D. Trabert, X. Y. Lai, S. Eckart, M. Kunitski, M. Schöffler, T. Jahnke, X. B. Bian, R. Dörner, and C. F. de Morisson Faria, Phys. Rev. A **102**, 013109 (2020).

[18] J. Itatani, J. Levesque, D. Zeidler, H. Niikura, H. Pépin, J. C. Kieffer, P. B. Corkum, and D. M. Villeneuve, Nature (London) **432**, 867 (2004).

[19] L. Ortmann, A. Al Shafey, A. Staudte, and A. S. Landsman, Phys. Rev. Lett. **127**, 213201 (2021).

[20] W. Xie, J. Yan, M. Li, C. Cao, K. Guo, Y. Zhou, and P. Lu, Phys. Rev. Lett. **127**, 263202 (2021).

[21] L. J. Zipp, A. Natan, and P. H. Bucksbaum, Optica **1**, 361 (2014).

[22] X. Gong, C. Lin, F. He, Q. Song, K. Lin, Q. Ji, W. Zhang, J. Ma, P. Lu, Y. Liu, H. Zeng, W. Yang, and J. Wu, Phys. Rev. Lett. **118**, 143203 (2017).

[23] P. Ge, M. Han, M. M. Liu, Q. Gong, and Y. Liu, Phys. Rev. A **98**, 013409 (2018).

[24] X. Song, G. Shi, G. Zhang, J. Xu, C. Lin, J. Chen, and W. Yang, Phys. Rev. Lett. **121**, 103201 (2018).

[25] M. Han, P. Ge, Y. Shao, Q. Gong, and Y. Liu, Phys. Rev. Lett. **120**, 073202 (2018).

[26] P. Ge, M. Han, Y. Deng, Q. Gong, and Y. Liu, Phys. Rev. Lett. **122**, 013201 (2019).

[27] Z. Guo, P. Ge, Y. Fang, Y. Dou, X. Yu, J. Wang, Q. Gong, and Y. Liu, Ultrafast Sci. **2022**, 1 (2022).

[28] J. Ullrich, R. Moshammer, A. Dorn, R. Dörner, L. Ph. H. Schmidt, and H. Schmidtböcking, Rep. Prog. Phys. **66**, 1463 (2003).

[29] M. Peters, T. T. Nguyen-Dang, E. Charron, A. Keller, and O. Atabek, Phys. Rev. A **85**, 053417 (2012).

[30] M. M. Liu, M. Han, P. Ge, C. He, Q. Gong, and Y. Liu, Phys. Rev. A **97**, 063416 (2018).

[31] W. Becker, F. Grasbon, R. Kopold, D. B. Miloševic, G. G. Paulus, and H. Walther, Adv. At. Mol. Opt. Phys. **48**, 35 (2002).

[32] D. B. Milošević, Phys. Rev. A **74**, 063404 (2006).

[33] M. Busuladžić, A. Gazibegović-Busuladžić, D. B. Milošević, and W. Becker, Phys. Rev. A **78**, 033412 (2008).

[34] M. Busuladžić, A. Gazibegović-Busuladžić, and D. B. Milošević, Phys. Rev. Lett. **103**, 043001 (2009).

[35] Z. Guo, Y. Fang, P. Ge, X. Yu, J. Wang, M. Han, Q. Gong, and Y. Liu, Phys. Rev. A **104**, L051101 (2021).

[36] M. Han, P. Ge, Y. Shao, M. M. Liu, Y. Deng, C. Wu, Q. Gong, and Y. Liu, Phys. Rev. Lett. **119**, 073201 (2017).

[37] M. Han, P. Ge, J. Wang, Z. Guo, Y. Fang, X. Ma, Y. Deng, H. J. Wörner, Q. Gong, and Y. Liu, Nat. Photonics **15**, 765 (2021).

[38] D. G. Arbó, K. L. Ishikawa, K. Schiessl, E. Persson, and J. Burgdörfer, Phys. Rev. A **81**, 021403(R) (2010).

[39] M. Kunitski, N. Eicke, P. Huber, J. Köhler, S. Zeller, J. Voigtsberger, N. Schlott, K. Henrichs, H. Sann, F. Trinter, L. Ph. H. Schmidt, A. Kalinin, M. S. Schöffler, T. Jahnke, M. Lein, and R. Dörner, Nat. Commun. **10**, 1 (2019).

[40] S. Eckart, Phys. Rev. Res. **2**, 033248 (2020).

[41] D. Trabert, S. Brennecke, K. Fehre, N. Anders, A. Geyer, S. Grundmann, M. S. Schöffler, L. Ph. H. Schmidt, T. Jahnke, R. Dörner, M. Kunitski, and S. Eckart, Nat. Commun. **12**, 1697 (2021).

[42] M. D. Feit, A. J. Fleck Jr., and A. Steiger, J. Comput. Phys. **47**, 412 (1982).

[43] I. Dreissigacker and M. Lein, Chem. Phys. **414**, 69 (2013).